Journal of Materials Chemistry A

Accepted Manuscript

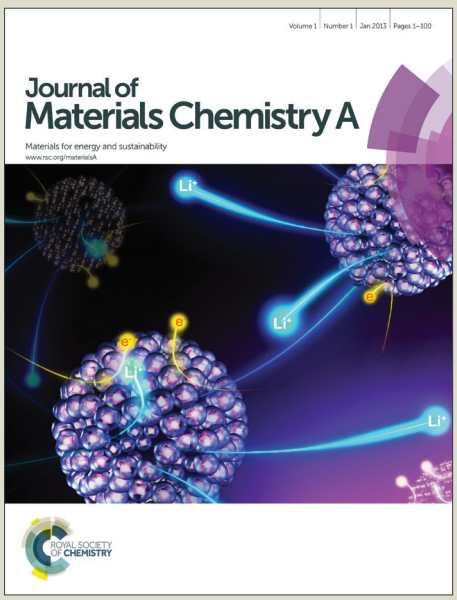

ROYAL SOCIETY OF CHEMISTRY

www.rsc.org/materialsA

High-Performance Supercapacitors Based on MnO_2 Tube-in-Tube Arrays

Xue-Feng Lu, An-Liang Wang, Han Xu, Xu-Jun He, Ye-Xiang Tong, and Gao-Ren Li*

MOE Laboratory of Bioinorganic and Synthetic Chemistry, KLGHEI of Environment and Energy Chemistry, School of Chemistry and Chemical Engineering, Sun Yat-sen University, Guangzhou 510275, China

E-mail: ligaoren@mail.sysu.edu.cn

Abstract

The MnO_2 tube-in-tube arrays supported on carbon fiber cloth (MnO_2 TTAs/CFC) were designed and synthesized. As a robust integrated 3D electrode with high utilization rate and fast ion transport, the MnO_2 TTAs/CFC exhibits high areal specific capacitance (Csp) of 322 $mF \cdot cm^{-2}$ (~1007 F/g for MnO_2 at 0.125 A/g) and superior cycling stability (96.4% retention of the initial Csp after 2000 cycles) at a high scan rate of 100 mV/s. The assembled flexible all-solid-state symmetric supercapacitors (SSCs) based on MnO_2 TTAs/CFC electrodes show a high volumetric energy density of 0.073 $mW \cdot h/cm^3$ at the power density of 25 W/kg and high cycling stability (96.4% retention of the initial Csp after 2000 cycles).This study demonstrates that the 3D MnO_2 TTAs/CFC electrodes hold great potential for the flexible energy storage devices.

Keywords: MnO_2, tube-in-tube, carbon fiber cloth, solid-state symmetric supercapacitor, energy storage

Introduction

Recently, supercapacitors (SCs) with desirable properties of high power density and high cycling stability have attracted great interest because they have been considered as one of the most promising candidates for the next-generation energy storage devices.[1-5] However, the low energy density of SCs greatly limits their wide applications.[6-9] To further enhance the energy density of SCs, it is crucial to design the favorable microstructures for electrodes with fast ion and electron transports and high utilization rate.[10-12] In the past decades, various hollow structures, such as hollow spheres, hollow prisms and nanotubes, have been designed and fabricated for the electrodes of SCs.[13] However, the multi-shelled hollow structures are rarely effectively synthesized for SCs, although they have shown obviously enhanced electrochemical properties compared to the simple hollow structures.[14] Inspired by these facts, researchers worldwide have devoted increasing endeavors to the rational design and synthesis of complex hollow structures.[15] The hollow structures with higher complexity are expected to offer the exciting opportunities for both fundamental studies and practical applications.[16] The tube-in-tube arrays (TTAs), constructed from an inner tube within an outer tube (gap exists between the inner and outer tubes), exhibit multiple channels and surfaces and thus will exhibit much improved performance for SCs. However, to the best of our knowledge, there are rarely reports on the synthesis of TTAs for SCs. The development of a simple strategy to effectively fabricate the TTAs of metal oxides is still a huge challenge.

In this study, we develop a simple template-assisted electrodeposition for the synthesis of MnO_2 TTAs on carbon fiber cloth (MnO_2 TTAs/CFC). MnO_2 has been widely thought to be one of the most promising materials for SCs because of its low cost, high abundance, large theoretical specific capacitance (C_{sp}), and environment friendly.[17-20] The MnO_2 TTAs/CFC as electrodes will show a huge potential for SCs because of the well-defined multiple surfaces and channels. As we all known, the diffusion distance of electrolyte into electrode is usually ~20 nm in depth,[21] which means that the material under 20 nm is "dead" or "inactive" as far as the electrochemical energy storage is concerned. In addition, the pursuance of high mass-loading of active materials usually leads to the increase of "dead volume" of electrode, which is not accessible for electrolyte permeating and thus results in low utilization ratio of electrode materials.[22]

Here the designed MnO_2 TTAs/CFC significantly improve the mass loading of active material, meanwhile the void space in MnO_2 TTAs/CFC will avoid effectively "dead volume" and thus will improve the ion transport and the utilization rate of electrode material. Because of unique structures, the designed MnO_2 TTAs/CFC electrodes exhibit high C_{sp} (322 mF/cm^2, 1007 A/g) and outstanding cycling stability (95.1% retention of the initial C_{sp} after 2000 cycles at a high scan rate of 100 mV/s). The flexible all-solid-state symmetric supercapacitors (SSCs) are assembled basing on the MnO_2 TTAs/CFC electrodes and they exibit high volumetric energy density of 0.073 mWh/cm^3 (11.3 Wh/kg) at the power density of 25.0 W/kg and high cycling stability (96.4% retention of the initial C_{sp} after 2000 cycles).

Experimental Section

All chemical reagents used in this study were analytical (AR) grade. Electrodeposition was carried out in a simple three-electrode cell via HDV-7C transistor potentiostatic apparatus, and the graphite electrode (spectral grade, 1.8 cm^2), carbon fiber cloth (CFC, 0.7×0.5 cm^2) and Ag/AgCl electrode were utilized as counter electrode, working electrode and reference electrode, respectively. Before electrodeposition, the CFC was successively rinsed with ethanol and distilled water in ultrasonic bath for 5 min, and repeatedly cleaned three times. Firstly, ZnO MRAs were electrodeposited on the CFC in 0.01 M $Zn(NO_3)_2$+0.05 M NH_4NO_3 solution at 0.4 mA/cm^2 at 70 °C for 90 min (ZnO MRAs/CFC). Secondly, MnO_2 was electro-deposited on ZnO MRAs in solution of 0.02 M $Mn(CH_3COO)_2$+0.20 M Na_2SO_4 at 0.45 V (vs. Ag/ AgCl) for 1 min and ZnO@MnO_2 MRAs/CFC were obtained. Thirdly, ZnO layer was further electrodeposited on the ZnO@MnO_2 MRAs for 15 min to form ZnO@MnO_2@ZnO MRAs/CFC. Fourthly, MnO_2 layer were further deposited on the ZnO@MnO_2@ZnO MRAs to form multilayered ZnO@MnO_2@ZnO@MnO_2 MRAs. Finally, the fabricated ZnO@MnO_2@ZnO@MnO_2 MRAs were immersed in 2.5 wt% aqueous ammonia for 3 h to remove ZnO completely and the MnO_2 TTAs/CFC were fabricated. In addition, for the comparative study, the MnO_2 STAs/CFC electrodes were fabricated via the similar synthesis method by etching ZnO@MnO_2/CFC MRAs in 2.5 wt% aqueous ammonia for 2 h.

Electrochemical measurements of the MnO_2 TTAs/CFC and MnO_2 STAs/CFC electrodes were carried

out in a standard three-electrode electrolytic cell in 1.0 M Na_2SO_4 aqueous solution. A graphite electrode and saturated calomel electrode (SCE) were used as counter electrode and reference electrode, respectively. Cyclic voltammometry and chronopotentiometric measurements were performed on a CHI 760E electrochemical workstation (CH instruments, Inc.) to determine the electrochemical properties of the MnO_2 TTAs/CFC and MnO_2 STAs/CFC electrodes. Before testing, a dorp of ethonal was dropped on the working electrode to ensure it was throughly wetted by electrolyte.

Before assembling all-solid-state flexible SSC device, a piece of filter paper (TF45-NKK, 40 μm) and two pieces of MnO_2 TTAs/CFC electrodes were immersed into LiCl/PVA gel electrolyte for 4 min. Then the all-solid-state SSC device with a sandwiched structure was assembled by two pieces of MnO_2 TTAs/CFCs as electrodes and a piece of TF45-NKK membrane as a separator in the middle (MnO_2 TTAs/CFC-SSC). The LiCl/PVA gel electrolyte was prepared as following: 6 g polyvinyl clcohol (PVA) power was dissolved in 60 mL distilled water at 85 ^{0}C under stirring. After PVA power was completely dissolved, 12.6 g LiCl was added into the PVA solution under vigorous stirring until the formation of a homogeneous sticky solution. The solution was then cooled at room temperature, and the solution finally became a clear and transparant gel.

Electrochemical measurements of the assembled all-solid-state MnO_2 TTAs/CFC-SSC devices were carried out in a two-electrode system. The cyclic voltammometry and chronopotentiometric measurements were carried out on a CHI 760E electrochemical workstation (CH instruments, Inc.) to determine the electrochemical performance of the devices.

Results and Discussion

The fabrication procedure of MnO_2 TTAs/CFC electrode is shown in Scheme 1a and 1b and the details are described in the Experimental Section. The precursors, such as ZnO microrod arrays(MRAs)/CFC, ZnO@MnO_2 MRAs/CFC, ZnO@MnO_2@ZnO MRAs/CFC, and ZnO@MnO_2@ZnO@MnO_2 MRAs/CFC all were orderly fabricated and their SEM images are shown in Figure S2a, S2b, S2c, and S2d, respectively. It can be seen that the ZnO MRAs are successfully fabricated on CFC as shown Figure S2a. The MnO_2 and ZnO wraps favorably share the surfaces of ZnO MRAs and the morphology of MRAs were well kept

as shown in Figure S2b-d. After completely dissolving ZnO in 2.5 wt% aqueous ammonia, we successfully fabricate the MnO_2 tube-in-tube arrays (TTAs)/CFC as shown in Figure 1a-b, which show the microstructures of TTAs with different magnifications. To demonstrate the universality of this fabrication method, the MnO_2 TTAs also can be successfully fabricated on Ti substrate as shown in Figure S3.

To further study the tube-in-tube structure of MnO_2 TTAs, TEM image, HRTEM and SAED pattern were further characterized. The tube-in-tube microstructure is clearly seen from its broken structure and vertical view as shown in Figure 1c and 1d, respectively. The wall thickness of outer tube is ~140 nm, and that of the inner tube is ~80 nm. The gap space between two walls is ~140 nm. The diameter of outer tube is ~600 nm and that of inner tube is ~200 nm. The various void spaces in MnO_2 TTAs will effectively improve the specific surface area and transport of electroactive species. Meanwhile, the void spaces can effectively avoid "dead volume" of electrode, and thus will obviously improve the utilization efficiencies of electrode materials. In addition, the mass loading of MnO_2 TTAs is significantly improved compared with the single nanotubes. In the HRTEM image shown in Figure 1e-f, the spacings between the adjacent fringes are 0.24 or 0.46 nm, which are in conformity with the (401) and (810) lattice spacings of MnO_2 (PDF #44-0142), respectively. The selected area electron diffraction (SAED) pattern shown in the inset in Figure 1e indicates the polycrystalline nature of MnO_2 TTAs. For the comparative study, MnO_2 single-walled tube arrays on CFC (MnO_2 STAs/CFC) were also synthesized by the similar method and their SEM, TEM, HRTEM and SAED images were measured as shown in Figure S4 and S5.

X-ray photoelectron spectroscopy (XPS) was used to further characterize the MnO_2 TTAs/CFC. The survey XPS spectrum of MnO_2 TTAs/CFC in Figure S6 shows three elements (Mn, O and C) existing in the sample, which confirms that the ZnO has been dissolved completely. The signals of Mn and O come from MnO_2, and the C signal comes from CFC. Figure 2a shows high resolution XPS spectrum of Mn 2p. The Mn $2p_{3/2}$ and Mn $2p_{1/2}$ peaks are centered at 642.0 and 653.8 eV, respectively, indicating that element Mn in the prepared samples is present in the chemical state of Mn(IV). The binding energy separation of the above two peaks is ~11.8 eV, which is in good agreement with the reported value for MnO_2.[23] Additionally, the multiplet splitting Mn 3s peaks are also useful for determining the oxidation state of Mn

because the peak separation of electrons in the core level with unpaired electrons in the valence band level is caused by the electron exchange interaction upon photoelectron ejection. As shown in Figure 2b, the energy separation between the two components of Mn 3s multiplet is 4.8 eV, which is consistent with the MnO_2 reported before.[24] The high resolution O1s spectrum is shown in Figure S7, which shows the O 1s spectrum of the MnO_2 TTAs/CFC can be deconvoluted into two components, suggesting the presence of two kinds of oxygen-containing species. The bands at 529.82 eV and 531.17 eV can be assigned to the oxygen bond of O^{2-} (O-Mn) and O^{2-} (O-H), respectively. The O^{2-} (O-Mn) can be attributed to MnO_2, and O^{2-} (O-H) can be attributed to the adsorbed H_2O in the MnO_2 TTAs/CFC. In addition, the element analysis by XPS spectra reveals that the atomic ratio of Mn and O is about 1: 2. Therefore, based on the above results, the obtained manganese oxide can be identified as MnO_2.

Cyclic voltammetry (CV) has been widely used to characterize the capacitive behavior of electrode material. Figure 3a shows the typical CVs of MnO_2 TTAs/CFC at different scan rates from 5 to 100 mV/s in 1.0 M Na_2SO_4 aqueous solution. These CVs all exhibit parallelogram-like shapes even at a high scan rate of 100 mV/s, indicating the continuous fast and reversible redox reactions taking place.[24] The dependence of areal C_{sp} on scan rate is shown in Figure 3b, which shows the MnO_2 TTAs/CFC owns much higher areal C_{sp} than MnO_2 STAs/CFC at different scan rates, indicating the advantages of tube-in-tube structures in the MnO_2 TTAs/CFC for supercapacitive performance. Figure 3c and S9 show the galvano-static charge/discharge (GCD) curves at various current densities from 0.125 to 3.75 A/g and 6.25 to 37.5 A/g, respectively. Both the profiles of charge/discharge curves and the symmetries reveal good capacitive characteristics. The areal C_{sp} of MnO_2 TTAs/CFC is achieved 322 mF/cm^2 at 0.125 A/g, corresponding to the mass C_{sp} of 1007 F/g (for MnO_2), which is much higher than those reported for MnO_2 electrodes.[5] The dependence of areal C_{sp} on the discharge current density is shown in Figure 3d, which also shows the areal C_{sp} of MnO_2 TTAs/CFC is much higher than that of MnO_2 STAs/CFC. As we all know, the excellent cycle ability is crucial for real SC operations. Here the long-term cycle stability of the MnO_2 TTAs/CFC is evaluated by conducting 2000-cycle CV test at a high scan rate of 100 mV/s, and the results are shown in Figure 3e. The MnO_2 TTAs/CFC owns outstanding cycling stability and exhibit 95.1% retention of the

initial C_{sp} after 2000 cycles at 100 mV/s, while the MnO_2 STAs/CFC only show 74.4% retention of the initial C_{sp} because of the structure collapse that is shown in Figure S11. The structure of MnO_2 TTAs/CFC is almost unchanged after 2000-cycle testing as shown in Figure S12, indicating the stable structure of MnO_2 TTAs/CFC. Therefore, the MnO_2 TTAs/CFC as electrode shows great potential for SCs.

The electrochemical impedance spectroscopy (EIS) measurements are used to investigate the electrochemical reaction kinetics in electrodes. Nyquist plots of MnO_2 TTAs/CFC electrodes before and after 2000 cycles are measured at the open circuit potential in the frequency range from 0.01 to 10^5 Hz and they are shown in Figure 3f. They both consist of two partially overlapped semicircles in the high and medium frequency regions and inclined lines in the low-frequency domains. Usually, at the high frequency, the intersection of the curve at the real part indicates the resistance of the bulk solution resistance (R_s),[25] and the semicircle diameter reflects the charge-transfer resistance (R_{ct}),[26] while the linear region corresponds to the Warburg diffusion process (W), reflecting the ion diffusion into the bulk of active materials.[27] For MnO_2 TTAs/CFC, the R_s and R_{ct} both are small, indicating that the low charge transfer resistance enables fast redox reactions and easier electron transport, and thus improves their specific capacity. After 2000-cycle test, the R_{ct} of MnO_2 TTAs/CFC almost keeps unchanged and it is still small, indicating the stable structure of MnO_2 TTAs/CFC. But the R_{ct} of MnO_2 STAs/CFC becomes much bigger after 2000-cycle test as shown in Figure S13 because of the structure collapse (see Figure S11). This is concordant with the results of the above cycle-ability testing.

The superior supercapacitive performance of the MnO_2 TTAs/CFC can be attributed to the porous structure of CFC and the unique tube-in-tube morphology of MnO_2 TTAs as shown schematically in Figure S14. The merits of MnO_2 TTAs/CFC as electrodes for SCs are illustrated as following: (*i*) The CFC can act as conductivity framework, in which the interconnected carbon fibers and porous structure will provide fast transport paths for electrons and electrolyte ions as shown in Figure S14a. It also acts as the flexible substrates because of their mechanical flexibility, which are highly important for the upcoming portable flexible devices, such as roll-up displays, wearable computers, and medical implants;[28] (*ii*) The tube-in-tube structures can significantly improve the mass-loading of MnO_2, meanwhile the hollow struc-

ture and void space between the two tubes can avoid effectively the "dead volume", and thus improve the utilization efficiencies of electrode materials as shown in Figure S14b; (*iii*) The hollow and void spaces in MnO_2 TTAs can serve as an "ion reservoir" to facilite the transportation of electrolyte ions, and can well buffer volume change to avoid structure collapse of electrodes during the charge/discharge process; (*iv*) The MnO_2 TTAs can provide multiple channels and surfaces for the electrochemical reactions and the penetration of ions into electrode material because of the hollow structures in tubes and gaps between inner and outer tubes. Therefore, the above merits are crucial for the superior supercapacitive performance of MnO_2 TTAs/CFC.

To demonstrate the potential of the MnO_2 TTAs/CFC electrodes for SCs, the flexible all-solid-state symmetric supercapacitors (SSC) devices based on MnO_2 TTAs/CFC electrodes were assembled (denoted as MnO_2 TTAs/CFC-SSCs) as illstrated in Figure 4a. When two device units were connected in series and we found that they could drive a red light-emitting diode (LED, 1.5 V) for more than 60 s after charging at 2.8 A/g for 10 s as shown in Figure 4b. To study the performance, CVs of an all-solid-state MnO_2 TTAs/CFC-SSC from 5 to 100 mV/s were measured and they were shown in Figure 4c. These curves all exhibit parallelogram-like shapes, suggesting good capacitive behavior of the assembled SSC device.[29] The areal C_{sp} of the all-solid-state MnO_2 TTAs/CFC-SSC shows 42.4 mF/cm^2 at 5 mV/s. The dependence of areal C_{sp} of the MnO_2 TTAs/CFC-SSC on scan rates is plotted in Figure S15, which shows the MnO_2 TTAs/CFC-SSC owns much higher areal C_{sp} than MnO_2 STAs/CFC-SSC at various scan rates. In order to further evaluate the performance of the device, we performed the GCD test at different current densities as shown in Figure 4d. The shapes of GCD curves at different current densities all tend to triangle-like curves, and the discharge curves are nearly linear and symmetric with the corresponding charge counterparts, suggesting the rapid I-V response and good electrochemical reversibility.[30] The areal C_{sp} of MnO_2 TTAs/CFC-SSC achieves 81.6 mF/cm^2 at 62.5 mA/g, which is much higher than that of the MnO_2 STAs/CFC-SSC (35.8 mF/cm^2) at the same current density. The dependence of areal C_{sp} of MnO_2 TTAs/CFC-SSC on current density is plotted in Figure 4e, which also shows MnO_2 TTAs/CFC-SSC owns much higher areal C_{sp} than MnO_2 STAs/CFC-SSC at the different scan rates. Figure 4f shows Ragone plot

of MnO_2 TTAs/CFC-SSC calculated from the galvanostatic discharge curves. The all-solid-state MnO_2 TTAs/CFC-SSC shows a high volumetric energy density of 0.073 mWh/cm^3 (11.33 Wh/kg), which is much higher than 0.032 mWh/cm^3 (9.95 Wh/kg) of all-solid-state MnO_2 STAs-SSC at the same power density of 25 W/kg. The volumetric energy density of all-solid-state MnO_2 TTAs/CFC-SSC is also higher than the reported all-solid-state SCs, such as ZnO-based all-solid-state SCs,[31] carbon nanotube-based all-solid-state SCs,[32] TiN nanowire array-based all-solid-state SCs,[33] TiO_2@C-based all-solid-state SCs,[34] polymer-based all-solid-state SCs,[35] and graphen-based all-solid-state SCs.[36] The cycle ability of the all-solid-state MnO_2 TTAs/CFC-SSC device was tested at a high scan rate of 100 mV/s for 2000 cycles. After 2000 cycles, the all-solid-state MnO_2 TTAs/CFC-SSC device exhibits 96.4% retention of the initial C_{sp} as shown in Figure 4g, indicating a superior cycle ability at a high scan rate of 100 mV/s. In addition, the all-solid-state MnO_2 TTAs/CFC-SSC is highly flexible, and the device exhibits similar C_{sp} at the different bend angles as shown in Figure S16, indicating its potential to be used as a flexible energy storage device.

Conclusions

In conclusion, the 3D MnO_2 TTAs/CFC were successfully fabricated via ZnO template-assisted electro-deposition. The structures of MnO_2 TTAs/CFC provide fast transport paths for electrons and electrolyte ions and are highly beneficial to improve the mass loading and availability of active materials. The MnO_2 TTAs/CFC as a electrode shows high areal C_{sp} of 322 mF/cm^2 at 0.125 A/g and outstanding cycling stability (95.1% retention of the initial C_{sp} after 2000 cycles at a high scan rate of 100 mV/s). The assembled flexible all-solid-state MnO_2 TTAs-SSC exhibits high volumetric energy density of 0.073 mWh/cm^3, which is about 2.5 times as high as that of MnO_2 STAs-SSC, superior cycle stability (96.4% retention of the initial C_{sp} after 2000 cycles at 100 mV/s), and excellent flexibility. This work shows an important breakthrough in the design and fabrication of advanced electrode materials of metal oxide with tube-in-tube structures for SCs.

Acknowledgements

This work was supported by NSFC (51173212), National Basic Research Program of China (2015CB932304),

Natural Science Foundation of Guangdong Province (S2013020012833), Fundamental Research Fund for the Central Universities (13lgpy51), SRF for ROCS, SEM ([2012]1707), the Project of High Level Talents in Higher School of Guangdong Province, and Open-End Fund of Key Laboratory of Functional Inorganic Material Chemistry (Heilongjiang University), Ministry of Education.

References

1. a) Y. He, W. Chen, X. Li, Z. Zhang, J. Fu, C. Zhao and E. Xie, *ACS Nano* 2013, **7**, 174; b) Z. Wang, Z. Zhu, J. Qiu, S. Yang, *J. Mater. Chem. C* 2014, **2**, 1331; G. D. Moon, J. B. Joo and Y. Yin, *Nanoscale*2013, **5**, 11577.
2. a) Z. Yang, J. Deng, X. Chen, J. Ren and H. Peng, *Angew. Chem. Int. Ed.* 2013, **52**, 13453; b) L. Bao, J. Zang and X. Li, *Nano Lett.* 2011, **11**, 1215.
3. a) X. Wang, B. Liu, R. Liu, Q. Wang, X. Hou, D. Chen, R. Wang and G. Shen, *Angew. Chem. Int. Ed.* 2014, **53**, 1849; b) G. Wang, H. Wang, X. Lu, Y. Ling, M. Yu, T. Zhai, Y. Tong and Y. Li, *Adv. Mater.* 2014, **26**, 2676.
4. a) Q. Lu, J. G. Chen and J. Q Xiao, *Angew. Chem. Int. Ed.* 2013, **52**, 1882; b) L. Hu, W. Chen, X. Xie, N. Liu, Y. Yang, H. Wu, Y. Yao, M. Pasta, H. N. Alshareef and Y. Cui, *ACS Nano* 2011, **5**, 8904.
5. a) G. Yu, L. Hu, M. Vosgueritchian, H. Wang, X. Xie, J. McDonough, X. Cui, Y. Cui and Z. Bao, *Nano Lett.* 2011, **11**, 2905; b) Y. Hou, Y. Cheng, T. Hobson and J. Liu, *Nano Lett.* 2010, **10**, 2727.
6. X. Peng, L. Peng, C. Wu and Y. Xie, *Chem. Soc. Rev.* 2014, **43**, 3303.
7. X. Xiao, T. Li, P. Yang, Y. Gao, H. Jin, W. Ni, W. Zhan, X. Zhang, Y. Cao, J. Zhong, L. Gong, W.-C. Yen, W. Mai, J. Chen, K. Huo, Y.-L. Chueh, Z. L. Wang and J. Zhou, *ACS Nano* 2012, **6**, 9200.
8. B. Liu, J. Zhang, X. Wang, G. Chen, D. Chen, C. Zhou and G. Shen, *Nano Lett.* 2012, **12**, 3005.
9. a) X. Xia, D. Chao, Z. Fan, C. Guan, X. Cao, H. Zhang and H. J. Fan, *Nano Lett.* 2014, **14**, 1651; b) C. Guan, X. Xia, N. Meng, Z. Zeng, X. Cao, C. Soci, H. Zhang and H. J. Fan, *Energy Environ. Sci.* 2012, **5**, 9085.
10. a) X. Xia, D. Chao, Z. Fan, C. Guan, X. Cao, H. Zhang and H. J. Fan, *Nano Lett.* 2014, **14**, 1651; b) C. Guan, X. Xia, N. Meng, Z. Zeng, X. Cao, C. Soci, H. Zhang and H. J. Fan, *Energy Environ. Sci.* 2012, **5**, 9085; c) G. Yu, L. Hu, N. Liu, H. Wang, M. Vosgueritchian, Y. Yang, Y. Cui and Z. Bao, *Nano Lett* 2011, **11**, 4438.
11. J. Jiang, Y. Li, J. Liu, X. Huang, C. Yuan and X. W. Lou, *Adv. Mater.* 2012, **24**, 5166.
12. X. Wang, X. Lu, B. Liu, D. Chen, Y. Tong and G. Shen, *Adv. Mater.* 2014, **26**, DOI: 10.1002/adma.201400910.
13. a) X. Wang, X. Lu, B. Liu, D. Chen, Y. Tong and G. Shen, *Adv. Mater.* **2014**, *26*, 4763; b) L. Yu, L. Zhang, H. Wu and X. W. Lou, *Angew. Chem. Int. Ed.* 2014, **53**, 3711; c) X. Xia, Z. Zeng, X. Li, Y. Zhang, J. Tu, C. F. Ng, H. Zhang and H. J. Fan, *Nanoscale* 2013, **5**, 6040.
14. a) H. T. Tan, X. Rui, H. Yu, W. Liu, C. Xu, Z. Xu, H. H. Hng and Q. Yan, *ACS Nano* 2014, **8**, 4004; b) Z. Zhao, H. Wu, H. He, X. Xu and Y. Jin, *Adv. Funct. Mater.* 2014, **24**, DOI: 10.1002/adfm.201400118.
15. a) M. Sathiya, A. Prakash, K. Ramesha, J-M. Tarascon and A. K. Shukla, *J. Am. Chem. Soc.* 2011, **133**, 16291; b) J.-H. Kim, K. Zhu, Y. Yan, C. L. Perkins and A. J. Frank, *Nano Lett.* 2010, **10**, 4099.

16. a) G. Zhang, B. Xia, C. Xiao, L. Yu, X. Wang, Y. Xie and X. W. Lou, *Angew. Chem. Int. Ed.* 2013, **52**, 8643; b) J. Zhao, J. Chen, S. Xu, M. Shao, Q. Zhang, F. Wei, J. Ma, M. Wei, D. G. Evans and X. Duan, *Adv. Funct. Mater.* 2014, **24**, 2938.

17. S. Chen, J. Zhu, X. Wu, Q. Han and X. Wang, ACS Nano 2010, **4**, 2822; J. Duay, S. Sherrill, Z. Gui, E. Gillette and S. B. Lee, *ACS Nano* 2013, **7**, 1200.

18. a) L. Peng, X. Peng, B. Liu, C. Wu, Y. Xie and G. Yu, *Nano Lett.* 2013, **13**, 2151; b) L. Yuan, X.-H. Lu, X. Xiao, T. Zhai, J. Dai, F. Zhang, B. Hu, X. Wang, L. Gong, J. Chen, C. Hu, Y. Tong, J. Zhou and Z. L. Wang, *ACS Nano* 2012, **6**, 656.

19. a) Z. Yu, B. Duong, D. Abbitt and J. Thomas, *Adv. Mater.* 2013, **25**, 3302; b) L.-F. Chen, Z.-H. Huang, H.-W. Liang, Q.-F. Guan and S.-H. Yu, *Adv. Mater.* 2013, **25**, 4746.

20. D. Kong, J. Luo, Y. Wang, W. Ren, T. Yu, Y. Luo, Y. Yang and C. Cheng, *Adv. Funct. Mater.* 2014, **24**, 3815.

21. C.-C. Hu, K.-H. Chang, M.-C. Lin and Y.-T. Wu, *Nano Lett.* 2006, **6**, 2690.

22. G. Yu, L. Hu, N. Liu, H. Wang, M. Vosgueritchian, Y. Yang and Y. Cui, Z. Bao, *Nano Lett.* 2011, **11**, 4438.

23. a) A. L. Reddy, M. M. Shaijumon, S. R. Gowda and P. M. Ajayan, *Nano Lett.* 2009, **9**, 1002; b) C. Zhu, S. Guo, Y. Fang, L. Han, E. Wang and S. Dong, *Nano Research* 2011, **4**, 648.

24. a) M. Toupin, T. Brousse and D. Belanger, *Chem. Mater.* 2004, **16**, 3184; b) Z. Su, C. Yang, B. Xie, Z. Lin, Z. Zhang, J. Liu, B. Li, F. Kang and C. P. Wong, *Energy Environ. Sci.* 2014, **7**, DOI: 10.1039/C4EE01195C.

25. a) R. Rakhi, W. Chen, D. Cha and H. Alshareef, *Nano Lett.* 2012, **12**, 2559; b) G. Zhang, W. Li, K. Xie, F. Yu and H. Huang, *Adv. Funct. Mater.* 2013, **23**, 3675.

26. P. Justin, S. K. Meher and G. R. Rao, *J. Phys. Chem. C* 2010, **114**, 5203.

27. L. Li, Y. Cheah, Y. Ko, P. Teh, G. Wee, C. Wong, S. Peng and M. Srinivasan, *J. Mater. Chem. A* 2013, **1**, 10935.

28. L. Li, Z. Wu, S. Yuan and X.-B. Zhang, *Energ. Environ. Sci.* 2014, **7**, 2101.

29. a) L. Li, Z. Wu, S. Yuan and X.-B. Zhang, *Energ. Environ. Sci.* 2014, **7**, 2101; b) Z. Su, C. Yang, B. Xie, Z. Lin, Z. Zhang, J. Liu, B. Li, F. Kang and C. P. Wong, *Energ. Environ. Sci.* 2014, **7**, 2652.

30. Z. Fan, J. Yan, T. Wei, L. Zhi, G. Ning, T. Li and F. Wei, *Adv. Funct. Mater.* 2011, **21**, 2366.

31. P. Yang, X. Xiao, Y. Li, Y. Ding, P. Qiang, X. Tan, W. Mai, Z. Lin, W. Wu, T. Li, H. Jin, P. Liu, J. Zhou, C. P. Wong and Z. L. Wang, *ACS Nano* 2013, **7**, 2617.

32. a) M. Kaempgen, C. K. Chan, J. Ma, Y. Cui and G. Gruner, Nano Lett. 2009, **9**, 1872; b) Y. J. Kang, H. Chung, C.-H. Han and W. Kim, *Nanotechnology* 2012, **23**, 289501.

33. X. Lu, G. Wang, T. Zhai, M. Yu, S. Xie, Y. Ling, C. Liang, Y. Tong and Y. Li, *Nano Lett* 2012, **12**, 5376.

34. H. Zheng, T. Zhai, M. Yu, S. Xie, C. Liang, W. Zhao, S. C. I. Wang, Z. Zhang and X. Lu, *J. Mater. Chem. C* 2013, **1**, 225.

35. C. Meng, C. Liu, L. Chen, C. Hu and S. Fan, *Nano Lett* 2010, **10**, 4025.

36. a) Y. Xu, Z. Lin, X. Huang, Y. Liu, Y. Huang and X. Duan, *ACS Nano* 2013, **7**, 4042; b) S. Wang, B. Pei, X. Zhao and R. A. Dryfe, *Nano Energy* 2013, **2**, 530.

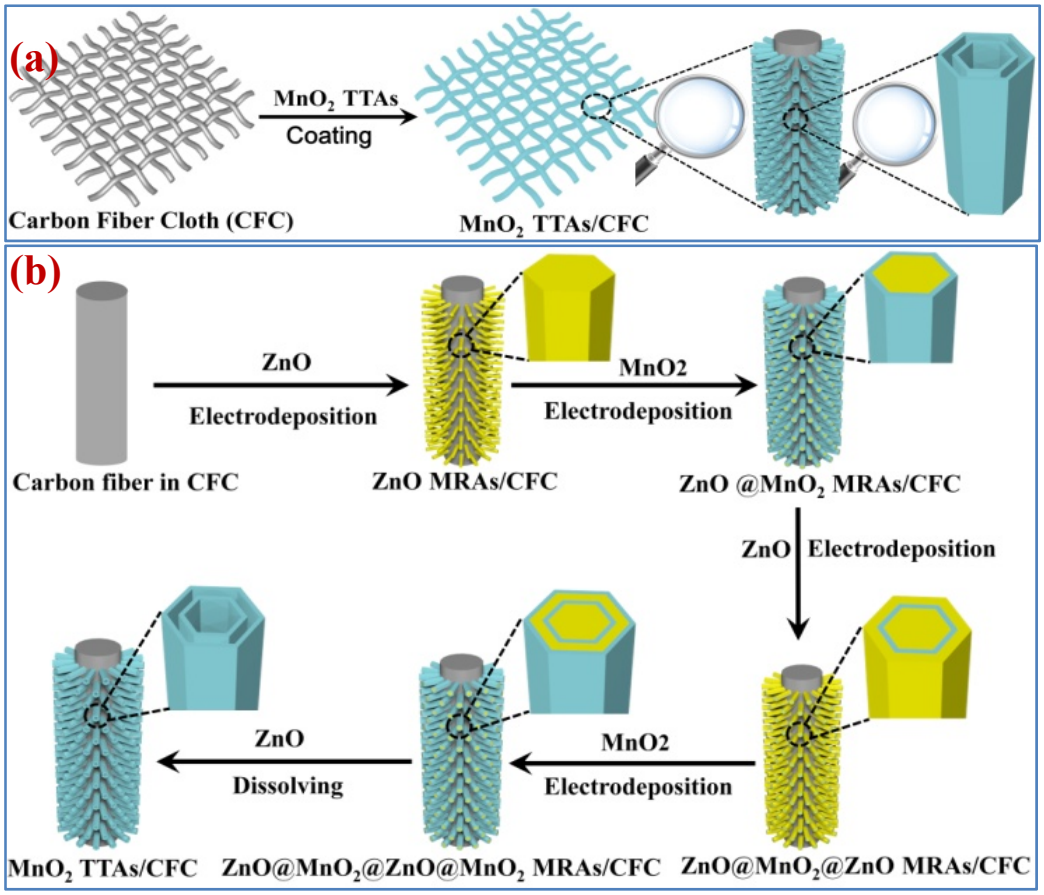

Scheme 1. (a) The overview of the fabrication of MnO_2 TTAs on CFC (MnO_2 TTAs/CFC); (b) Schematic illustration for the fabrication process of MnO_2 TTAs/CFC by ZnO template-assisted electrodeposition.

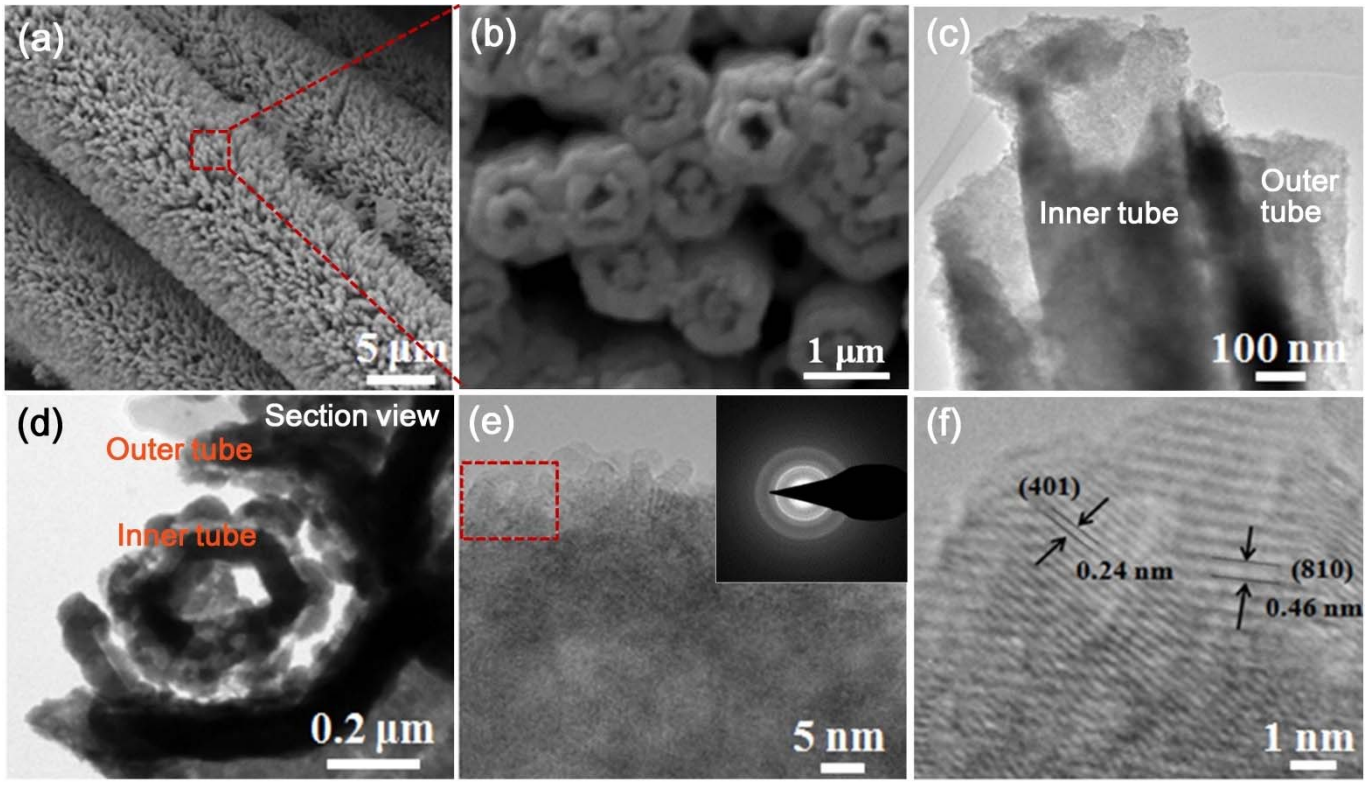

Figure 1. (a-b) SEM images of MnO_2 TTAs/CFC with different magnifications; (c) TEM image of the profile view of tube-in-tube structure; (d) TEM image of the section view of tube-in-tube structure; (e-f) HRTEM images of tube wall with different magnifications.

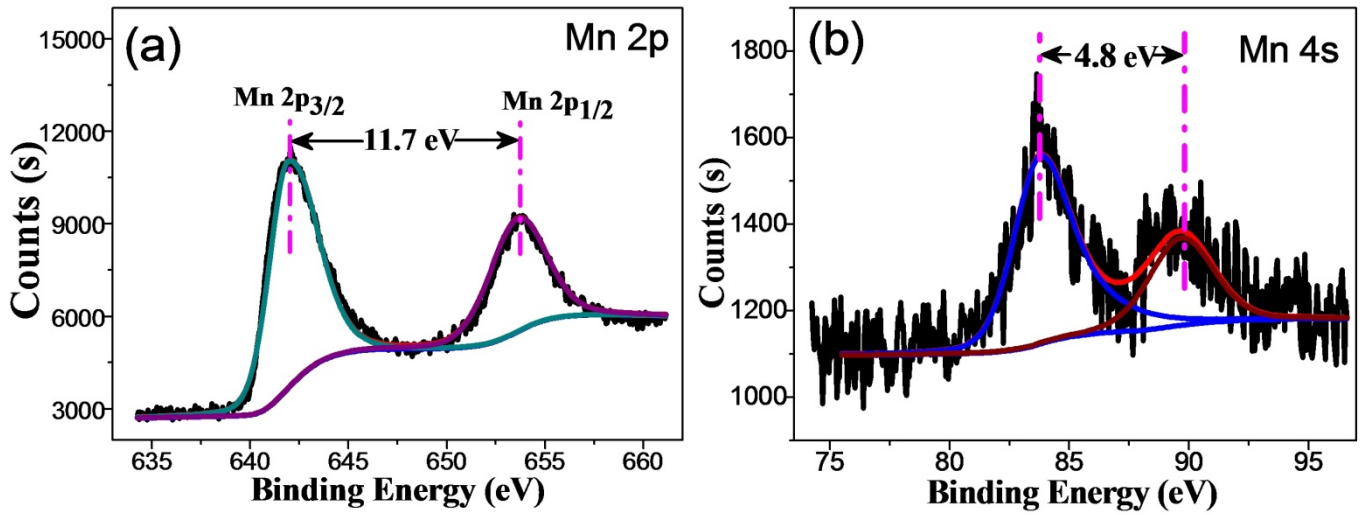

Figure 2. XPS spectra of (a) Mn 2p and (b) Mn 4s of the MnO_2 TTAs/CFC.

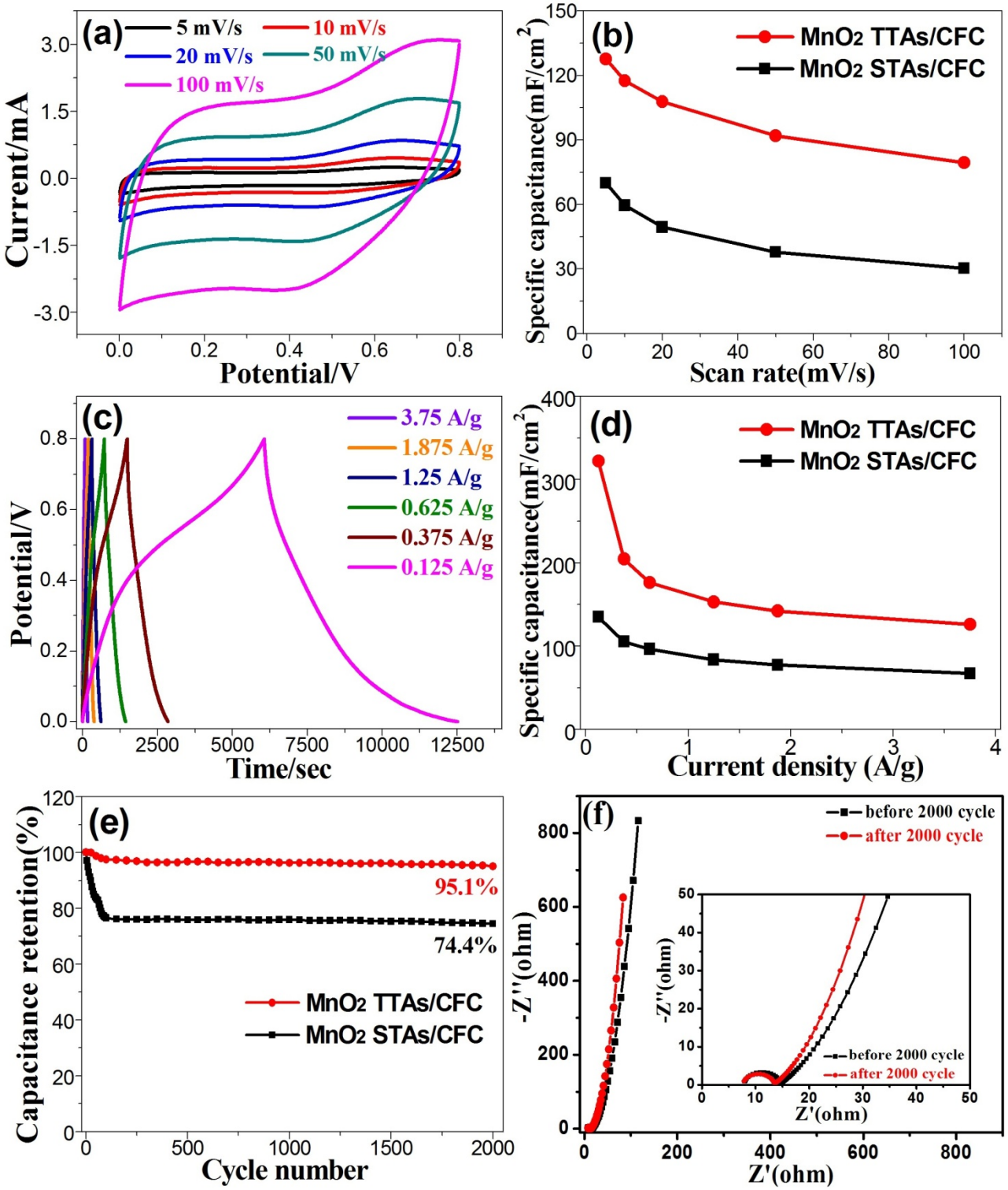

Figure 3. (a) CVs of the MnO_2 TTAs/CFC at the different scan rates; (b) The dependence of C_{sp} on scan rate for MnO_2 TTAs/CFC and MnO_2 STAs/CFC; (c) GCD curves of the MnO_2 TTAs/CFC at the different current densities; (d) The dependence of C_{sp} on the current densities for MnO_2 TTAs/CFC and MnO_2 STAs/CFC; (e) Cycle lives of the MnO_2 TTAs/CFC and MnO_2 STAs/CFC; (f) Nyquist plots of the MnO_2 TTAs/CFC before and after 2000 cycles.

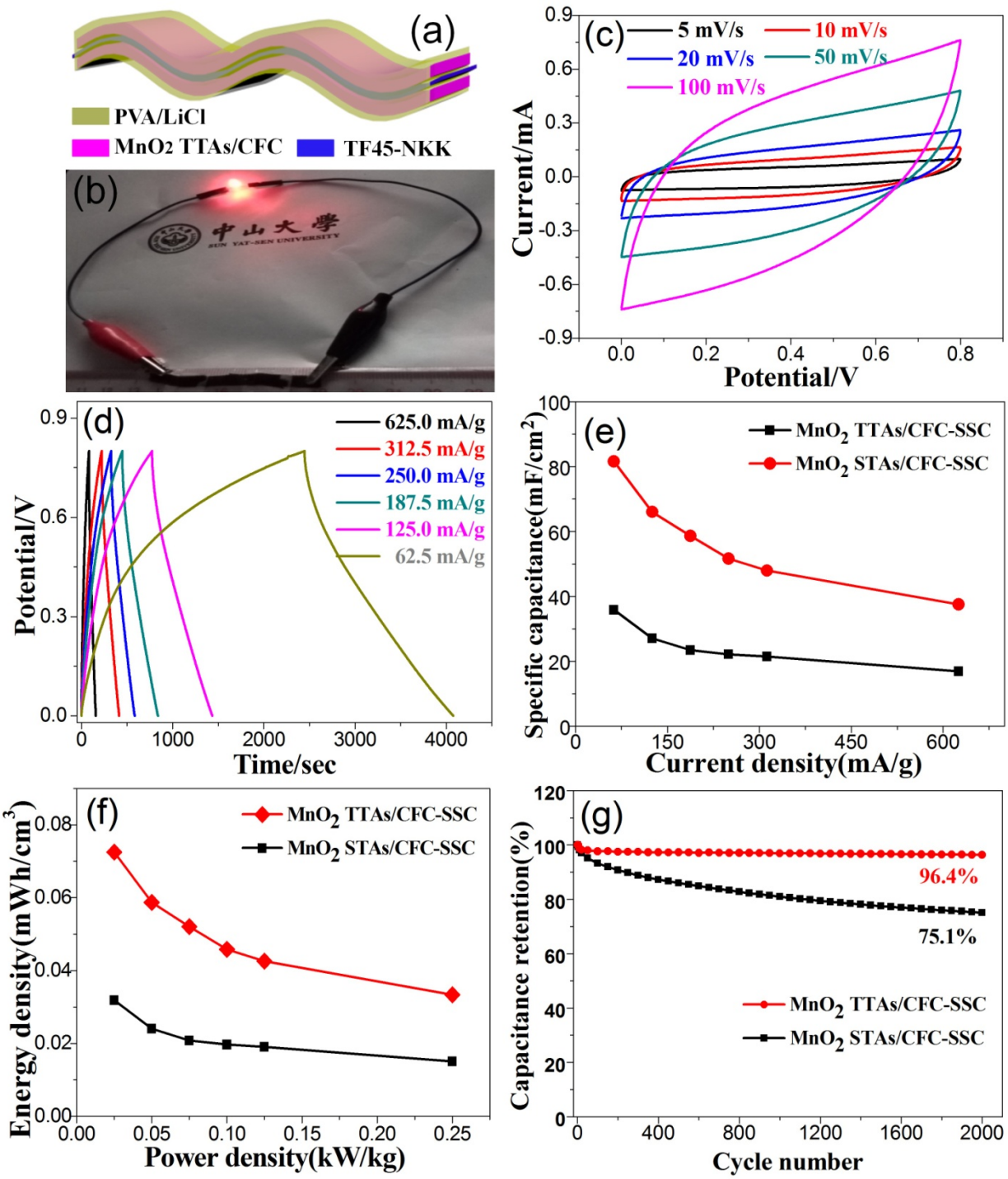

Figure 4. (a) Schematic illustration for the assemble of all-solid-state MnO_2 TTAs/CFC-SSC that are composed of MnO_2 TTAs/CFC electrodes and TF45-NKK membrane (the solid electrolyte is PVA/LiCl); (b) RED light-emitting diode (LED) lighting demonstration, with the diode driven by a simple fabricated SSC device; (c) CVs of all-solid-state MnO_2 TTAs/CFC-SSC at different scan rates; (d) GCD curves of MnO_2 TTAs/CFC-SSC at different current densities; (e) The dependence of C_{sp} on current densities for MnO_2 TTAs/CFC-SSC and MnO_2 STAs/CFC-SSC; (f) Ragone plots and (g) cycle performance of MnO_2 TTAs/CFC-SSC and MnO_2 STAs/CFC-SSC.

TOC Graphic